Title
Electron beam-induced current imaging with two-angstrom resolution.

Authors
Mecklenburg, Matthew
Hubbard, William A
Lodico, Jared J
et al.

Publication Date
2019-12-01

DOI
10.1016/j.ultramic.2019.112852

Peer reviewed

Electron beam-induced current imaging with two-angstrom resolution

Matthew Mecklenburg

Core Center of Excellence in Nano Imaging (CNI), University of Southern California, Los Angeles, California, 90089, U.S.A.

William A. Hubbard, Jared J. Lodico, B. C. Regan

Department of Physics and Astronomy, University of California, Los Angeles, CA 90095, U.S.A.

California NanoSystems Institute, University of California, Los Angeles, CA 90095, U.S.A.

Abstract

An electron microscope's primary beam simultaneously ejects secondary electrons (SEs) from the sample and generates electron beam-induced currents (EBICs) in the sample. Both signals can be captured and digitized to produce images. The off-sample Everhart-Thornley detector that is common in scanning electron microscopes (SEMs) can detect SEs with low noise and high bandwidth. However, the transimpedance amplifiers appropriate for detecting EBICs do not have such good performance, which makes accessing the benefits of EBIC imaging at high-resolution relatively more challenging. Here we report lattice-resolution imaging via detection of the EBIC produced by SE emission (SEEBIC). We use an aberration-corrected scanning transmission electron microscope (STEM), and image both microfabricated devices and standard calibration grids.

Keywords: `aberration-correction, transmission electron microscopy, secondary electrons, STEM, EBIC`

1. Introduction

Lattice resolution (< 1 nm) imaging with scanning transmission electron microscopy (STEM) in its standard mode was first demonstrated by Crewe and Wall in 1970 [1]. Since this milestone was achieved, efforts have been ongoing to extend such resolution to the auxiliary imaging and spectroscopic modes available to STEM instruments. Lattice resolution secondary electron imaging [2], electron energy loss spectroscopy [3], and energy dispersive X-ray spectroscopy [4] were first demonstrated in 1990, 2007, and 2010 respectively. Atomic-resolution (< 0.1 nm) versions of the same milestones were reached in 2009 [5], 2008 [6], and 2010 [7] respectively.

The subject of this paper, secondary electron electron beam induced current (SEEBIC) imaging, is closely related to the secondary electron imaging just mentioned, but also to electron-beam induced current (EBIC) imaging. In standard EBIC imaging [8], the rastering STEM beam creates electron-hole pairs in the sample that are then separated in a local electric field, such as might be found in a p-n junction. The region where the pairs are generated is electrically connected to a transimpedance amplifier (TIA), which collects either the electrons or the holes, depending on the side of the circuit to which the TIA is connected. Associating the measured current with the beam position creates the EBIC image.

In SEEBIC imaging, on the other hand, there is no intrinsic electric field; the image contrast is generated by the production of secondary electrons and their associated holes [9] (see Fig. 1 and accompanying text). If a direct current path exists from the charge generation region to the TIA, the TIA will collect more holes and the contrast will be positive. If the TIA is instead connected to an electrode that is neighboring, but not directly connected to the charge generation region, the ejected SEs (or associated tertiary electrons) can travel through the

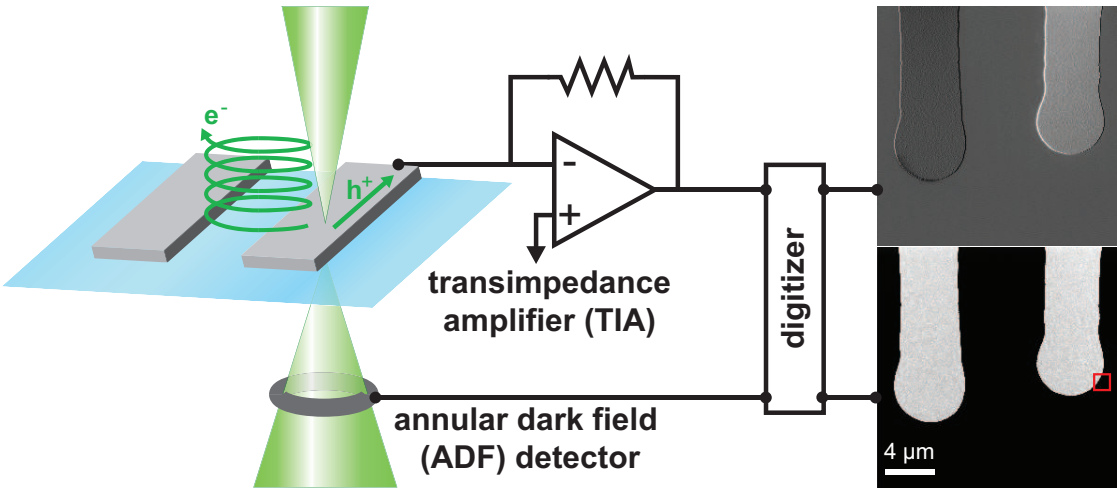

Figure 1: **Schematic of an experimental setup and corresponding low-magnification images.** A device consisting of two metal electrodes (each consisting of a 5 nm Ti adhesion layer covered with 25 nm of Pt) on a insulating, electron-transparent membrane is being imaged with scanning transmission electron microscopy (STEM). The lower signal chain generates the standard STEM annular dark field (ADF) image, which shows both contacts with the same contrast. The upper signal chain generates the SEEBIC image with its differential contrast: the electrode attached to the transimpedance amplifier (TIA) is bright while the other electrode is dark. A red box in the ADF image indicates the scale of the electrode-edge region shown in the leftmost frame of Fig. 2.

microscope vacuum to reach this neighboring electrode. In this instance the TIA measures a negative current and generates negative contrast. Relative to standard EBIC, SEEBIC signals are typically smaller [9], but they are found throughout a device, and not just in special regions that happen to support a non-zero electric field.

Standard SE imaging is, of course, the main imaging mode of the scanning electron microscope (SEM), and is sometimes employed in the TEM. In both cases SE liberated by the scanning electron beam are captured off-sample in a detector, and associating the measured SE signal with the beam position again produces the image. The off-sample detector most commonly used for SE was invented by Everhart and Thornley [10], and is a marvel of low-noise amplification. Using a kilovolt-scale positive potential, it accelerates the low energy ($\lesssim 10\,eV$) SE into a scintillator, producing light that is subsequently detected with a photomultiplier tube. As described already in the 1960 publication announcing this invention [10], detectors based on this architecture can have femtoampere (10^{-15} A) sensitivity with 10 MHz bandwidth. Compare these specifications with those of a modern TIA used for the detection of EBIC: the DLPCA-200 made by FEMTO Messtechnik GmbH and used in this study, for instance, has an integrated input noise current (rms) of 800 fA with 1.1 kHz bandwidth. These specifications indicate that, as a device for measuring electrical currents, the Everhart-Thornley detector is superior to a modern TIA by more than two orders-of-magnitude in both noise current spectral density *and* bandwidth. From a technological standpoint, detecting free charges in vacuum is clearly easier than detecting them in a metal wire.

Given that off-sample SE detectors outperform TIAs by orders-of-magnitude, and that atomic resolution imaging using SE was achieved only recently, the question then arises: is it possible to achieve lattice resolution with an EBIC-based technique? The purpose of this communication is to provide an answer in the affirmative, and to describe how the STEM imaging and sample parameters can be optimized to compensate for the fundamentally poor signal-to-noise performance of the TIA.

2. Experiment

Except for the data of Fig. 1, we used the TEAM 1 microscope at the National Center for Electron Microscopy (NCEM) at the Molecular Foundry in Lawrence Berkeley National Laboratory (LBNL). This microscope is a modified FEI

Titan 80-300 equipped with a CEOS hexapole-type probe corrector that provides full correction of 3rd order ($C_3 < 0.5\,\mu$m) and partial correction of 5th order ($C_5 < 0.5$ mm) spherical aberrations. Annular dark field (ADF) signals were collected with a Fischione Model 3000 ADF detector, and digitized by a Gatan Digiscan II to 12-bit precision simultaneously with the EBIC signal from a DLPCA-200. Electrical connection to the sample was made with a biasing sample holder (Hummingbird Scientific). The images of Fig. 1 were acquired using the FEI Titan 80-300 in the California NanoSystems institute at UCLA, which also has a Fischione Model 3000 ADF detector but does not have a corrector.

Both microscopes were operated at an accelerating voltage of 300 kV with a probe current of 200–300 pA. In probe-corrected microscopes a smaller accelerating voltage would likely give better SEEBIC performance, as the SE yield, and thus the signal, varies inversely with the beam energy [11, 9]. The large probe current was chosen as a compromise between having a small probe ($\lesssim 50$ pA is typical for high-resolution imaging) and a good signal-to-noise ratio in the EBIC channel (the EBIC signal is proportional to the beam current [9]). The data of Fig. 1 were acquired with a convergence angle $\alpha \simeq 9$ mrad, as is typical for high-resolution imaging with an uncorrected microscope. All other data were acquired with $\alpha \simeq 17$ mrad. For high-resolution imaging with a first generation spherical aberration corrector, $\alpha \simeq 25$ mrad would be standard, but with the less-demagnified source the smaller convergence angle more coherently fills the probe-forming second condenser aperture. Typical dwell times were 1.5–2.5 ms/pixel, which corresponds to 2–3 minutes for a 256×256 pixel image.

As SEEBIC imaging is most revealing in samples that contain multiple electrically-disconnected regions [9], we demonstrate lattice resolution imaging in actual devices featuring lithographically-defined metal electrodes. Figure 1 shows a basic experimental arrangement, where the device consists of two metal electrodes that have been defined via optical lithography and are facing each other across a 25 nm-thick silicon nitride membrane. The electrodes have identical thicknesses and thus give the same contrast in the ADF images, since they scatter the beam electrons into the ADF detector with equal efficiency. However, while they also generate secondary electrons (SEs) with equal efficiency, these same electrodes give opposite contrast in the EBIC images. Because the TIA is attached to one electrode and not the other, the SE signal actually changes sign between the electrodes. When the beam hits the electrode attached to the TIA, more SEs are generated than return to the electrode, and so the net (hole) current into the TIA is positive and gives bright contrast. When the beam hits the other electrode, some secondary and tertiary electrons reach the TIA's electrode (no holes do) and the net (electron) current into the TIA is negative, giving dark contrast. This SEEBIC image of Fig. 1 demonstrates one of the major strengths [9] of SEEBIC imaging relative to both standard STEM imaging and off-sample SE imaging: it reveals electrical connectivity.

The contrast reversal between the electrodes is not exact; the hole current in the electrode connected to the TIA has greater magnitude than the electron current generated from another electrode [9]. Thus when imaging at high spatial resolution or otherwise attempting to maximize the signal-to-noise ratio, it is generally best to image using the stronger hole signal. Under most circumstances this optimization presents no difficulties. If the feature of interest happens to be on or near an electrode not attached to the TIA, one can either switch the TIA to the electrode of interest, short the electrode of interest to the TIA's electrode, or add yet another TIA and thereby add another SEEBIC imaging channel.

3. Results

To demonstrate lattice resolution we first dropcast 5 nm diameter gold nanoparticles from a colloidal suspension (Ted Pella, part # 15702) onto a device with 5/25 nm Ti/Pt electrodes. The gold lattice provides a clean distance calibration standard, where a measured lattice parameter can be identified with a known distance with certainty. Such a standard is not available from the device itself, for in this case the three materials available are unsuitable. Although crystalline, the metal electrode materials might be alloyed, oxidized, or otherwise chemically altered from their pure, elemental forms during the fabrication processing. The Si_3N_4 support membrane is amorphous and thus has no well-defined lattice parameter. And the silicon wafer that frames the Si_3N_4 membrane, while a single crystal, is in no place sufficiently thin to allow lattice resolution imaging.

Two dropcast particles that have had their chemical identities confirmed as Au via energy dispersive

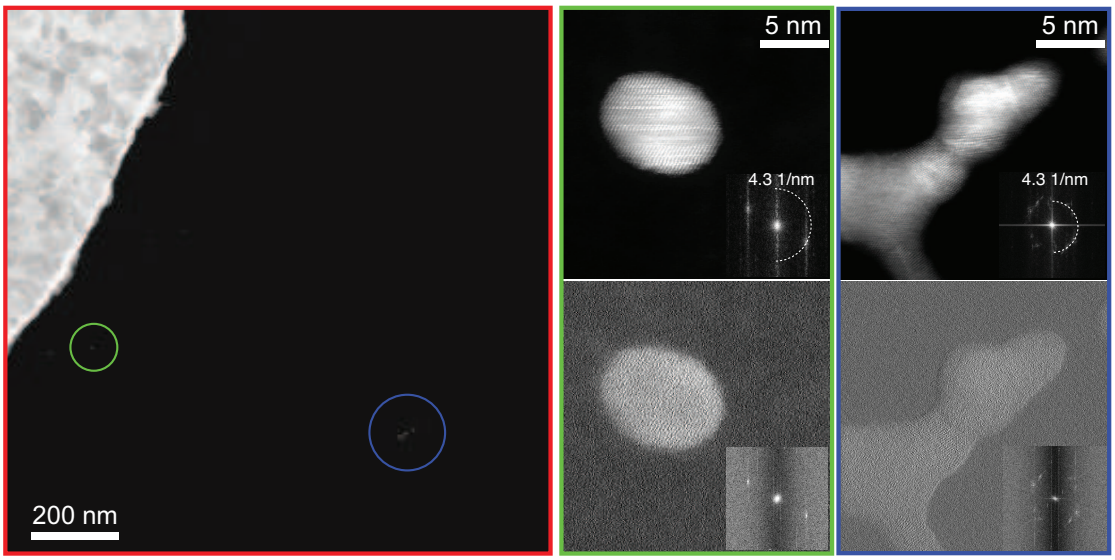

Figure 2: **ADF and SEEBIC images of regions adjacent to an electrode.** A Ti/Pt SEEBIC sense electrode has several gold nanoparticles nearby (left image, ADF). Two circled nanoparticles are shown at high-magnification (right images, indicated by the correspondingly colored frames). Both the ADF (upper row) and the SEEBIC images (lower row) show lattice resolution, as demonstrated by the peaks at the Au {111} spacing of 0.235 nm in the inset fast Fourier transforms (FFTs). As is observed generally and is the case here, the SEEBIC signal is stronger for nanoparticles closer to an electrode.

X-ray spectroscopy are highlighted in the leftmost frame of Fig. 2, one within 140 nm of the TIA's sense electrode, and the other 840 nm away. In both cases, high-resolution images of these particles show the gold lattice in both the ADF and the EBIC channels. Fast Fourier transforms (FFTs) of the images identify the gold {111} Bragg peak at 4.25 nm^{-1}, which corresponds to an interplanar spacing of 0.235 nm [12]. For ADF and EBIC images acquired simultaneously, the images have strictly identical scaling.

Here the EBIC signals are positive, indicating the existence of a through-the-sample electrical path between the electrode and the nominally isolated nanoparticles. Although not well-characterized, the resistance of this connection is likely in the TΩ range. While such a connection is not robust enough to give a strong EBIC signal, it is, perhaps surprisingly, robust enough to give a net hole current. The contrast in the EBIC channel is smaller than that in the ADF channel, and it is decreasing with increasing distance from the sense electrode.

This decrease can be quantified. In the EBIC channel, the farther, dog-shaped particle generates 3× less contrast than the closer, round particle, which itself generates 3× less contrast than the sense electrode itself. In each case here 'contrast' is defined as the difference between the signal from the metal and that from the neighboring Si_3N_4. For comparison, in the ADF channel the farther, dog-shaped particle generates 1.5× more contrast than the closer, round particle, which generates 6× less contrast than the sense electrode itself. Thus, relative to ADF, the EBIC contrast is more sensitive to connectivity (and correspondingly to location), and less sensitive to the total thickness. To achieve the best possible EBIC signal-to-noise ratio and contrast, the region of interest should therefore be either part of the sense electrode, or electrically connected to it.

Imaging a 5/25 nm Ti/Pt sense electrode at higher magnification (Fig. 3) reveals that lattice resolution can be achieved not only in nanoparticles scattered over the device, but also in the actual components of the device itself. While the electrode is thin enough to be electron-transparent, the grains in the Pt layer are unlikely to be aligned with the grains of the Ti adhesion layer [9], which makes it very unlikely that both layers are aligned so as to allow the detection of lattice in the polycrystalline bulk. Consequently we image on the edge of the sense electrode, where the material is thinner than the nominal 30 nm.

To show both the electrode edge and the Si_3N_4

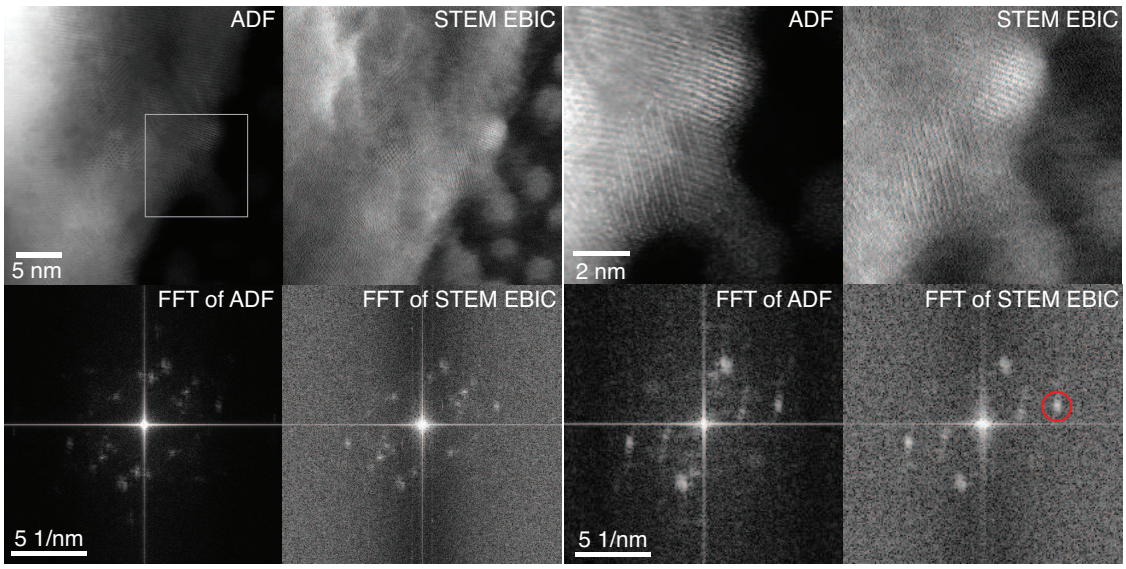

Figure 3: **Two pair of lattice-resolution ADF and SEEBIC images of Ti/Pt contacts on silicon nitride (top row), and the FFTs of these images (bottom row).** The real space images are acquired at two different magnifications (the grey box in the left ADF image indicates the full field of view of the right pair), but the FFTs are all shown with the same scale. A resolution of 200 pm is achieved, as indicated by the position of the circled peak in the FFT.

membrane, the first set of images (Fig. 3 left) have a slightly larger field of view. The ADF signal, being more sensitive to the sample's total thickness, shows the larger actual contrast variation between the electrode and the membrane. (These Fig. 3 images have had their display contrast levels set with the default 'sparse' auto-contrast function in version 2.3 of Gatan's Digital Micrograph software.) The EBIC signal, on the other hand, shows less actual contrast change as the electrode gets thicker. Thus the EBIC image can better exploit the 8-bit gray-scale display range available: it reveals fine details that are nearly invisible in the ADF image, such as nanoparticles adjacent to the electrode on the Si_3N_4 membrane. An excellent insulator, the membrane itself gives little SE signal, and produces only a small EBIC background in comparison to a conducting support (see e.g. Fig 4 and discussion).

Higher-magnification images of the same region (Fig. 3 right) make the lattice obvious, even in the real space images. Again the ADF contrast is stronger, but the similarity between the ADF and the EBIC images, despite the completely different contrast mechanisms, indicates a common root cause. In a classical (e.g. Rutherford) model, the ADF contrast is generated by the nuclear cores, which scatter beam electrons more strongly at smaller impact parameters. In the corresponding model of the EBIC contrast, the probability of SE emission varies with the sample's electron density, which is also greater nearer the nuclei. In more precise language one can say that the lattice signal in the SEEBIC image is evidence that SE are produced by inner-shell excitations, which correspond to larger energy scales [13] than the peak (< 10 eV) of the SE distribution [11, 9], and which are not de-localized [14, 15]. Thus both ADF and EBIC techniques can image the crystal lattice as defined by the positions of the nuclear cores. Further complexities of generating SEs at atomic resolution are discussed in [16], particularly how screening can dampen states near the Fermi energy and decrease high resolution contrast from lower-Z elements such as oxygen.

Finally we show that, while desirable, the device structure is not necessary for lattice resolution SEEBIC imaging: a simple TEM grid can be used in place of the device. For a test sample we use a standard carbon diffraction grating replica on a copper Gilder grid, with Au/Pd shadowing (Ted Pella part # 607), such as is commonly used for magnification calibration. Images of the gold/palladium (Fig. 4 top) show lattice in both the ADF and the EBIC channels. Because of its low atomic number Z, the

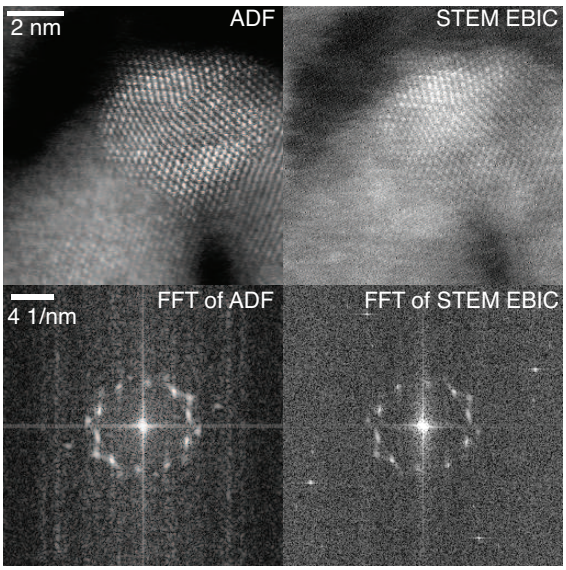

Figure 4: **ADF and SEEBIC images of the Pd/Au of a standard magnification calibration (TEM grid) sample, along with the FFTs of each image.** The Bragg reflections in the FFTs indicate a resolution of 200 pm. The apparent reflections at 11 nm^{-1} (which would correspond to an interplanar spacing of 90 pm) are due to 60 Hz pickup by the EBIC detection circuit.

carbon ($Z = 6$) film is less effective at scattering beam electrons than the bulk gold ($Z = 79$) and palladium ($Z = 46$), and thus it is not evident in the ADF image. The (conducting) carbon film is, however, visible in the EBIC image, because SEEBICs are generated more effectively from surfaces than from the bulk [9].

The corresponding FFTs (Fig. 4 bottom) show that both channels are detecting the same lattice, with a characteristic inter-plane spacing of 200 pm. The EBIC image shows some additional peaks that look as if they correspond to scattering angles about twice those of the main lattice peaks. These peaks are spurious and due to AC line noise. The noise is small and, if desired, could be easily removed from the image by masking the spurious peaks in reciprocal space and performing the inverse FFT. None of the data presented in this paper have had any such filtering applied.

4. Acknowledgments

This work was supported by National Science Foundation (NSF) award DMR-1611036, by NSF Science and Technology Center (STC) award DMR-1548924 (STROBE), and by the UCLA PSEIF. Work at the Molecular Foundry was supported by the Office of Science, Office of Basic Energy Sciences, of the U.S. Department of Energy under Contract No. DE-AC02-05CH11231. The authors acknowledge the use of instruments at the Electron Imaging Center for NanoMachines supported by NIH 1S10RR23057 and the CNSI at UCLA.

[1] A. V. Crewe, J. Wall, J. Langmore, Visibility of single atoms, science 168 (3937) (1970) 1338–1340.

[2] J. Liu, J. M. Cowley, High-angle ADF and high-resolution SE imaging of supported catalyst clusters, Ultramicroscopy 34 (1-2) (1990) 119–128.

[3] M. Bosman, V. J. Keast, J. L. Garcia-Munoz, A. J. D'Alfonso, S. D. Findlay, L. J. Allen, Two-dimensional mapping of chemical information at atomic resolution, Physical Review Letters 99 (8) (2007) 086102.

[4] A. J. D'Alfonso, B. Freitag, D. Klenov, L. J. Allen, Atomic-resolution chemical mapping using energy-dispersive X-ray spectroscopy, Physical Review B 81 (10) (2010) 100101.

[5] Y. Zhu, H. Inada, K. Nakamura, J. Wall, Imaging single atoms using secondary electrons with an aberration-corrected electron microscope, Nature Materials 8 (10) (2009) 808.

[6] D. A. Muller, L. F. Kourkoutis, M. Murfitt, J. H. Song, H. Y. Hwang, J. Silcox, N. Dellby, O. L. Krivanek, Atomic-scale chemical imaging of composition and bonding by aberration-corrected microscopy, Science 319 (5866) (2008) 1073–1076.

[7] M. Watanabe, M. Kanno, E. Okunishi, Atomic-resolution elemental mapping by EELS and XEDS in aberration corrected STEM, JEOL News 45 (8).

[8] H. J. Leamy, Charge collection scanning electron microscopy, Journal of Applied Physics 53 (6) (1982) R51–R80. doi:10.1063/1.331667.

[9] W. A. Hubbard, M. Mecklenburg, H. L. Chan, B. C. Regan, STEM imaging with beam-induced hole and secondary electron currents, Physical Review Applied 10 (4) (2018) 044066.

[10] T. E. Everhart, R. F. M. Thornley, Wide-band detector for micro-microampere low-energy electron currents, Journal of scientific instruments 37 (7) (1960) 246.

[11] M. S. Chung, T. E. Everhart, Simple calculation of energy distribution of low-energy secondary electrons emitted from metals under electron bombardment, Journal of Applied Physics 45 (2) (1974) 707–709. doi:10.1063/1.1663306.

[12] I.-K. Suh, H. Ohta, Y. Waseda, High-temperature thermal expansion of six metallic elements measured by dilatation method and X-ray diffraction, Journal of Materials Science 23 (2) (1988) 757–760. doi:10.1007/BF01174717.

[13] R. F. Egerton, Limits to the spatial, energy and momentum resolution of electron energy-loss spectroscopy, Ultramicroscopy 107 (8) (2007) 575–586. doi:10.1016/j.ultramic.2006.11.005.

[14] A. Howie, Recent developments in secondary electron imaging, Journal of Microscopy 180 (3) (1995) 192–203. doi:10.1111/j.1365-2818.1995.tb03678.x.

[15] H. G. Brown, A. J. D'Alfonso, L. J. Allen, Secondary electron imaging at atomic resolution using a focused

coherent electron probe, Physical Review B 87 (5) (2013) 054102. doi:10.1103/PhysRevB.87.054102.

[16] J. Ciston, H. G. Brown, A. J. D'Alfonso, P. Koirala, C. Ophus, Y. Lin, Y. Suzuki, H. Inada, Y. Zhu, L. J. Allen, L. D. Marks, Surface determination through atomically resolved secondary-electron imaging, Nature Communications 6 (2015) 7358. doi:10.1038/ncomms8358.